

Nanoscale Film Thickness Gradients Printed in Open Air by Spatially Varying Chemical Vapor Deposition

Abdullah H. Alshehri, Jhi Yong Loke, Viet Huong Nguyen, Alexander Jones, Hatameh Asgarimoghaddam, Louis-Vincent Delumeau, Ahmed Shahin, Khaled H. Ibrahim, Kissan Mistry, Mustafa Yavuz, David Muñoz-Rojas, and Kevin P. Musselman*

Nanoscale films are integral to all modern electronics. To optimize device performance, researchers vary the film thickness by making batches of devices, which is time-consuming and produces experimental artifacts. Thin films with nanoscale thickness gradients that are rapidly deposited in open air for combinatorial and high-throughput (CHT) studies are presented. Atmospheric pressure spatial atomic layer deposition reactor heads are used to produce spatially varying chemical vapor deposition rates on the order of angstroms per second. ZnO and Al₂O₃ films are printed with nm-scale thickness gradients in as little as 45 s and CHT analysis of a metal-insulator-metal diode and perovskite solar cell is performed. By testing 360 Pt/Al₂O₃/Al diodes with 18 different Al₂O₃ thicknesses on one wafer, a thicker insulator layer (≈7.0 nm) is identified for optimal diode performance than reported previously. Al₂O₃ thin film encapsulation is deposited by atmospheric pressure chemical vapor deposition (AP-CVD) on a perovskite solar cell stack for the first time and a convolutional neural network is developed to analyze the perovskite stability. The rapid nature of AP-CVD enables thicker films to be deposited at a higher temperature than is practical with conventional methods. The CHT analysis shows enhanced stability for 70 nm encapsulation films.

1. Introduction

Nanoscale coatings are integral components of all modern electronics, including display technologies, diodes, solar cells, batteries, and smart windows. In R&D settings, researchers must vary the thickness of thin films to optimize device performance. This typically involves making several batches of devices, each

with a different film thickness, and this process must be repeated for each film present in the device. In addition to being time-consuming, this iteration of material synthesis and device fabrication results in experimental artifacts due to uncontrolled differences in experimental conditions. These challenges can be addressed by using combinatorial and high-throughput (CHT) techniques.^[1] In CHT approaches, a thin film is produced whose properties (in this case, thickness) vary across its surface. Multiple devices can then be produced at different locations on the film surface and compared without batch-to-batch variation, making the technique faster and more reliable. This approach also significantly reduces the time and material costs during experimentation. In addition to CHT analysis, films with thickness gradients present an opportunity for novel functionality.

Nanoscale films with thickness gradients have been produced using vacuum-based techniques. Physical vapor deposition has been used to produce thickness gradients,^[2] and gas flows have been controlled in chamber-based atomic layer deposition and chemical vapor deposition systems to produce nanoscale thickness gradients.^[3–5] A summary of some reported combinatorial thickness-gradient films and methods^[2–4,6–12] are presented in Table S1 in the Supporting Information. While useful in some cases, these

A. H. Alshehri, J. Y. Loke, A. Jones, H. Asgarimoghaddam, L.-V. Delumeau, A. Shahin, Dr. K. Ibrahim, K. Mistry, Prof. M. Yavuz, Prof. K. P. Musselman
Department of Mechanical and Mechatronics Engineering
University of Waterloo
200 University Ave. West, Waterloo N2L 3G1, Canada
E-mail: kevin.musselman@uwaterloo.ca

A. H. Alshehri, J. Y. Loke, A. Jones, H. Asgarimoghaddam, A. Shahin, Dr. K. Ibrahim, K. Mistry, Prof. M. Yavuz, Prof. K. P. Musselman
Waterloo Institute for Nanotechnology
University of Waterloo
200 University Ave. West, Waterloo N2L3G1, Canada

 The ORCID identification number(s) for the author(s) of this article can be found under <https://doi.org/10.1002/adfm.202103271>.

A. H. Alshehri
Department of Mechanical Engineering
Prince Sattam bin Abdul Aziz University
Alkharj 11942, Saudi Arabia

Dr. V. H. Nguyen
Faculty of Electrical and Electronic Engineering
Phenikaa University
Hanoi 12116, Vietnam
Prof. D. M. Rojas
Univ. Grenoble Alpes
CNRS
Grenoble INP
LMGP
Grenoble 38000, France

DOI: 10.1002/adfm.202103271

vacuum-synthesized films are not suitable for cost-effective and high-throughput nanomanufacturing in atmosphere.

In contrast, atmospherically processed films with nanoscale thickness gradients are less developed. This is despite the fact that atmospheric processing is desired for many emerging technologies (flexible electronics, low-cost solar cells, wearable electronics, smart windows, etc.). Combinatorial atmospheric chemical vapor deposition and spray pyrolysis have been used to achieve composition and thickness gradients,^[9,13] however, the thicknesses were in the range of several hundreds of nanometers and reproducibility is an issue with spray pyrolysis, as the film quality depends on the droplet size and spray nozzle.^[14] A flow coating technique has been shown to produce a thickness gradient on the order of 10 nm for polymer films in atmosphere,^[10,11] but for most materials there are no demonstrations of nanometer-scale thin film thickness gradients.

Herein we introduce large-area thin films with thickness gradients on the nanometer scale that are manufactured using spatially varying atmospheric pressure chemical vapor deposition (AP-CVD) techniques. We rapidly print metal oxide films (Al_2O_3 , ZnO) with nanoscale thickness gradients in atmosphere and demonstrate their use in CHT studies of quantum-tunneling metal-insulator-metal (MIM) diodes and perovskite solar cells.

2. Results and Discussion

2.1. Atmospherically Printed Films with Nanoscale Thickness Gradients

Figure 1a illustrates the working principle of our dual atmospheric pressure spatial atomic layer deposition/chemical vapor

deposition (AP-SALD/CVD) system. Precursor and reactant vapors flow to a reactor head, which has parallel gas outlet channels along its bottom surface. The flows of the precursor and reactant vapors are isolated from each other by a curtain of inert nitrogen gas and exhaust channels (not shown in Figure 1a) located between the precursor and reactant channels: see ref. [15]. The substrate is placed under the atmospheric reactor with a small vertical separation (typically $d \approx 50 \mu\text{m}$) and is oscillated back and forth to expose the substrate to alternating reactant flows. Each point on the substrate moves underneath the precursor and adsorbs a molecular layer, after which the flow of inert gas removes any excess precursor. When the substrate moves under the reactant gas, which reacts with the layer of precursor on the substrate, a monolayer of the desired film is formed. By oscillating the substrate back and forth, we can deposit pinhole-free films with nanoscale thickness control. Spatial atomic layer deposition has been demonstrated for a variety of materials, substrates, and applications.^[16–19] When operating as an AP-CVD system, experimental conditions are selected such that the inert gas flow and exhaust strength are insufficient to prevent mixing of the precursor and reactant vapors during the oscillation of the substrate. Notably, this can be achieved by using a large reactor-substrate spacing.^[20,21] In AP-CVD, the reactions are no longer surface self-limited. Higher growth per cycle values are obtained for AP-CVD (typically on the order of 1 nm/cycle), but conformal pinhole-free films are still produced.^[22] This AP-CVD approach has been used to incorporate films into a variety of devices,^[22] and has sometimes been referred to as spatial CVD.^[23]

We have leveraged the fact that the AP-CVD deposition rate is influenced by the reactor-substrate spacing to produce nanoscale thickness gradients in ZnO and Al_2O_3 films. We varied the distance between the reactor head and the substrate

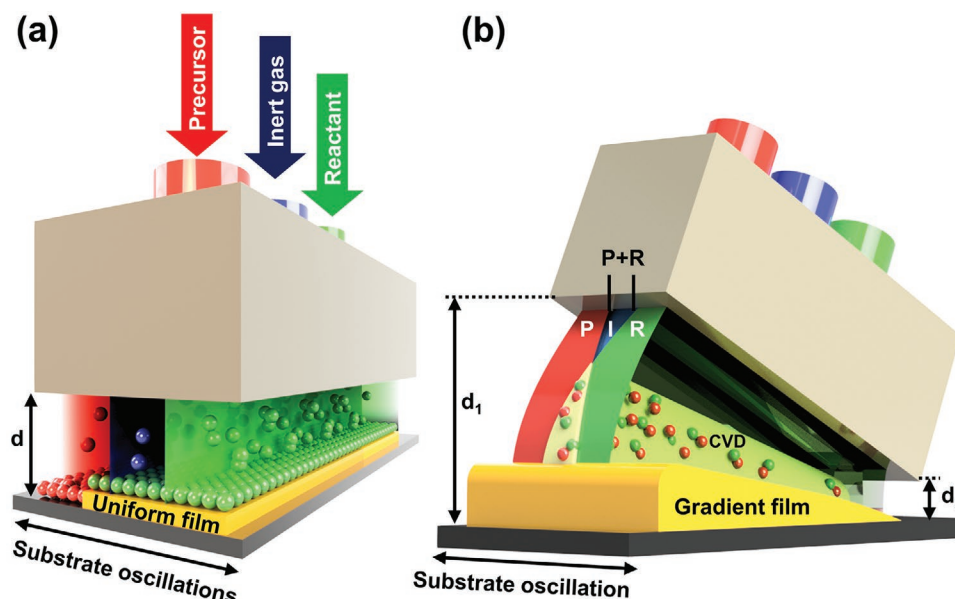


Figure 1. Variable reactor-substrate spacing approach to produce nanoscale film thickness gradients. a) Close-proximity AP-SALD approach with uniform reactor-substrate spacing d that isolates the precursor and reactant gases, resulting in surface self-limited ALD and uniform film thickness. b) By inclining the reactor head, we produce a variable reactor-substrate spacing d_1 , d_2 , causing mixing of the precursor and reactant to a varying extent, which results in a spatially varying chemical vapor deposition rate and a film with a thickness gradient.

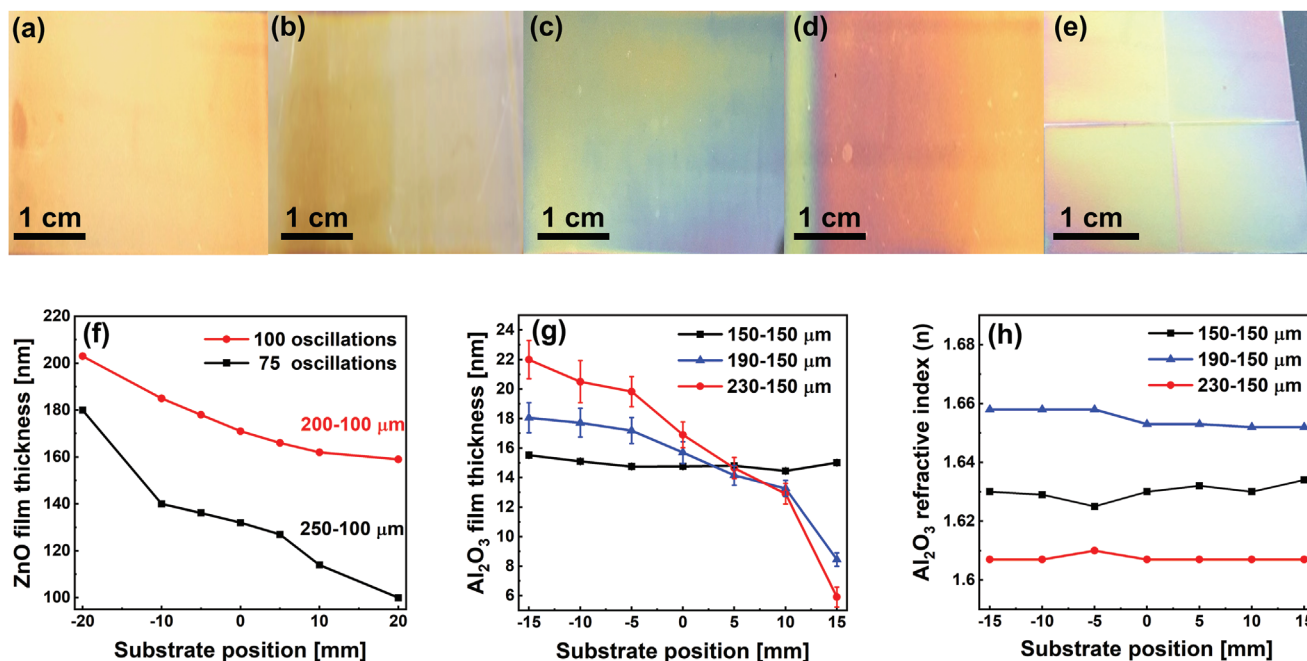


Figure 2. ZnO and Al₂O₃ thickness gradient films deposited with a variable reactor-substrate spacing. a) 95 nm uniform ZnO film deposited on glass using a uniform 100 μm reactor-substrate spacing and 75 substrate oscillations. b) 70–30 nm gradient ZnO film deposited on glass using a variable 150–90 μm reactor-substrate spacing and 40 substrate oscillations. c) 200–160 nm gradient ZnO film deposited on glass using a variable 200–100 μm reactor-substrate spacing and 100 substrate oscillations. d) 180–100 nm gradient ZnO film deposited on glass using a variable 250–100 μm reactor-substrate spacing and 75 oscillations. e) Four ITO substrates coated together with a 200–160 nm thickness gradient. f) Thickness of gradient ZnO films shown in (c,d). g) Thickness of gradient Al₂O₃ films produced on Si substrates by different reactor-substrate spacings. h) Refractive indices of the gradient Al₂O₃ films, measured along the gradient.

along the length of the reactor so that we had a reactor-substrate spacing of 90 to 150 μm (d_1) on one side and a larger spacing of 150 to 250 μm (d_2) on the other side, as shown in Figure 1b. More gas-phase mixing of the precursors occurs where the reactor-substrate spacing is larger, as shown on the left side of Figure 1b, resulting in an enhanced AP-CVD mode, which in turn yields a higher deposition rate. By varying the reactor-substrate spacing continuously across the substrate, a spatially varying deposition rate is expected that will result in a thickness gradient. We performed Computational Fluid Dynamics (CFD) analysis to simulate the phenomenon (see Figures S1–S4 and Table S2 in the Supporting Information).

We deposited zinc oxide films in this manner on 7 × 7 cm borosilicate glass substrates and 1.6 × 1.6 cm indium-tin-oxide/glass (ITO) substrates using diethylzinc (DEZ) and water. Figure 2a shows a 95 nm thick uniform ZnO film deposited on glass using a uniform reactor-substrate spacing of 100 μm and 75 substrate oscillations at an oscillation speed of 15 mm s⁻¹. The final thickness indicated a growth per cycle (GPC) of ≈0.63 nm/cycle (≈0.28 nm s⁻¹) (the DEZ precursor was flowed through one channel so one oscillation of the substrate back and forth was the equivalent of two precursor-reactant cycles). This GPC is consistent with AP-CVD growth rates reported previously.^[24] The properties of uniform ZnO films produced using similar conditions on this AP-SALD/CVD system have also been reported previously.^[24] Figure 2b shows a thickness gradient film obtained by setting the reactor-substrate spacing to 150 μm on the left side and 90 μm on the right side,

after 40 substrate oscillations at a speed of 15 mm s⁻¹. A clear gradient in the film thickness is observed, which was measured by ellipsometry to be 70 nm thick on the left of the film and 35 nm on the right, indicating GPCs of ≈0.87 and 0.43 nm/cycle, respectively. When depositions were repeated with the reactor-substrate spacing set to 200 and 250 μm on the left side and 100 μm on the right side, with 100 and 75 substrate oscillations at a speed of 15 mm s⁻¹, the resulting thickness ranges increased to 200–160 nm (Figure 2c) and 180–100 nm (Figure 2d), respectively, indicating GPCs from ≈0.7 to 1.2 nm/cycle, all consistent with AP-CVD. Figure 2e shows a 200–160 nm gradient produced on four ITO substrates using the same 200–100 μm reactor-substrate spacing, 75 substrate oscillations and an oscillation speed of 10 mm s⁻¹. This demonstrates the ability of the technique to produce thickness gradient films on typical substrate sizes used for device studies (e.g., solar cells and LEDs). Figure 2f shows thickness profiles for the ZnO films in Figure 2c,d, as measured by ellipsometry. The film thicknesses are observed to decrease continuously across the glass substrates. This agrees with the CFD simulation results in the Supporting Information.

Al₂O₃ films with thickness gradients were produced on 3 in. silicon substrates using trimethylaluminum (TMA) and water. The properties of uniform Al₂O₃ films produced on this AP-SALD/CVD system have been reported previously.^[21,24] A reactor-substrate spacing of 150 μm was maintained on the right side and 150, 190, or 230 μm on the left side. In all cases, the substrate was oscillated 20 times at a speed of 10 mm s⁻¹.

Thicknesses determined from ellipsometry measurements at various locations across the Al_2O_3 films are shown in Figure 2g. A uniform film thickness of 15 nm was observed when the reactor-substrate spacing was a constant 150 μm . When the left side of the reactor was raised to 190 μm , a thickness gradient ranging from 18–8 nm thick was produced. The gradient further increased to ≈ 22 –6 nm when the left side was raised to 230 μm . Three thickness measurements were performed perpendicular to the intended gradient for each substrate position and the standard deviation is indicated by the error bars in Figure 2g. There is some thickness variability in the perpendicular direction. This is expected as the reactor-substrate spacing may not stay perfectly constant throughout the travel distance due to how the substrate sits on the stage, non-uniformity in the substrate thickness, and/or levelling of the stage relative to the travel distance. But Figure 2g shows that the overall gradient is still consistent. For Al_2O_3 depositions, the TMA precursor was flowed through two channels, thus one oscillation is the equivalent of 4 precursor-reactant cycles. These depositions took ≈ 300 s, had GPCs that varied from ≈ 0.37 to 0.51 nm/cycle (0.1 to 0.14 nm s^{-1}) across the substrate, and demonstrate the ability of this approach to produce films with thickness gradients at the scale of nanometers in open-air in very short deposition times. In Figure 2h, refractive indices at 630 nm measured along the gradient films by ellipsometry are shown. These matched well with the 1.53–1.78 range reported previously for Al_2O_3 [21] and were constant along the thickness gradient. An Al_2O_3 gradient film with a larger thickness variation (86–7 nm) that was deposited using a variable 400–100 μm reactor-substrate spacing, 20 oscillations, and a speed of 30 mm s^{-1} was also characterized by ellipsometry and is shown in Figure S5 in the Supporting Information. For the larger thickness range, the refractive index decreases slightly with increasing thickness, consistent with previous reports for Al_2O_3 made by thermal ALD [25].

X-ray photoelectron spectroscopy (XPS) was performed on one of the Al_2O_3 thickness gradient films from Figure 2g (230–150 μm reactor-substrate spacing) to clarify the film composition and bonding. The XPS data is presented in Table S3 in the Supporting Information. The O/Al ratio is fairly constant across the Al_2O_3 thickness gradient film, with a slight increase at the thicker end. A carbon signal is present across the gradient and may be due to incomplete reaction of the trimethylaluminum or adventitious carbon on the surface of the sample,

resulting from storage in air and/or the XPS instrument.^[21,26,27] It is known that OH^- defects in Al_2O_3 can act as electron traps that facilitate the transport of electrons.^[21,28] We deconvoluted the O1s spectra for the different film thicknesses, as shown in Figure 3. The peaks at 531 and 532.3 eV correspond to Al-O and hydroxyl OH^- groups^[21], respectively. The contribution of the OH^- peak is high, as expected, as H_2O was used as the oxidant^[21]. Notably, the contribution of the OH^- peak was similar across the gradient film.

In a second approach, instead of tilting the reactor head physically, we modified the geometry of the channel in the reactor head to control the flow profile of the precursor vapor. The reactor was designed to deliver different amounts of precursor gas to different locations on the substrate. When the system is operated in AP-CVD conditions, a larger GPC is then expected at locations where more precursor is delivered, due to a higher molar flow, which increases mixing of the precursor and reactant. Figure 4a illustrates the working principle of this method where the precursor channel (P) is designed with a slant to vary the rate of delivery of the precursor vapor (more precursor is delivered to the left side of the substrate in Figure 4a). This approach allows a specific gradient profile to be built into the reactor and simplifies the deposition process by allowing a uniform reactor-substrate spacing to be used. With this approach, we also avoid the loss of precursor that can occur with tilting of the reactor head in the first method.

Figure 4b shows an internal view of the reactor head design illustrating the distribution of the channels. The intricate design of the inner channels is complicated if not impossible to be produced using conventional machining. However, such customized reactor designs can easily be fabricated owing to the possibilities offered by 3D printing.^[29] The reactor head contains two different precursor channels – uniform and gradient. The uniform channel is based on the normal channel design and produces films with uniform thickness when the reactor-substrate spacing is uniform. It can be used to deposit a uniform film before switching the precursor flow to the gradient channel. This ensures that the reactor-substrate spacing is uniform and that any gradients produced are defined by the design of the gradient channel and not unintended tilting of the reactor. When depositing with either of the precursor channels, we flowed inert gas through the channel that was not in use to prevent precursor or reactant gas from entering it.

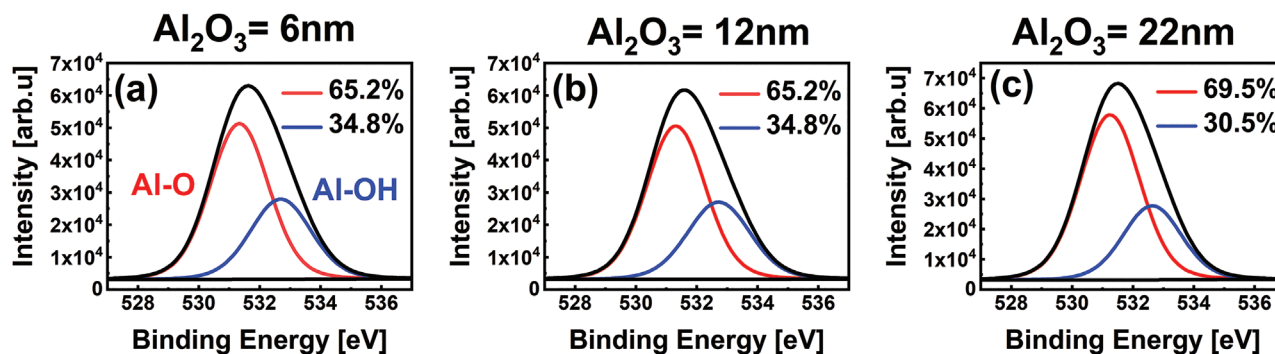


Figure 3. O1s XPS spectra of an Al_2O_3 thickness gradient film measured at different thicknesses: a) 6 nm, b) 12 nm, c) 22 nm.

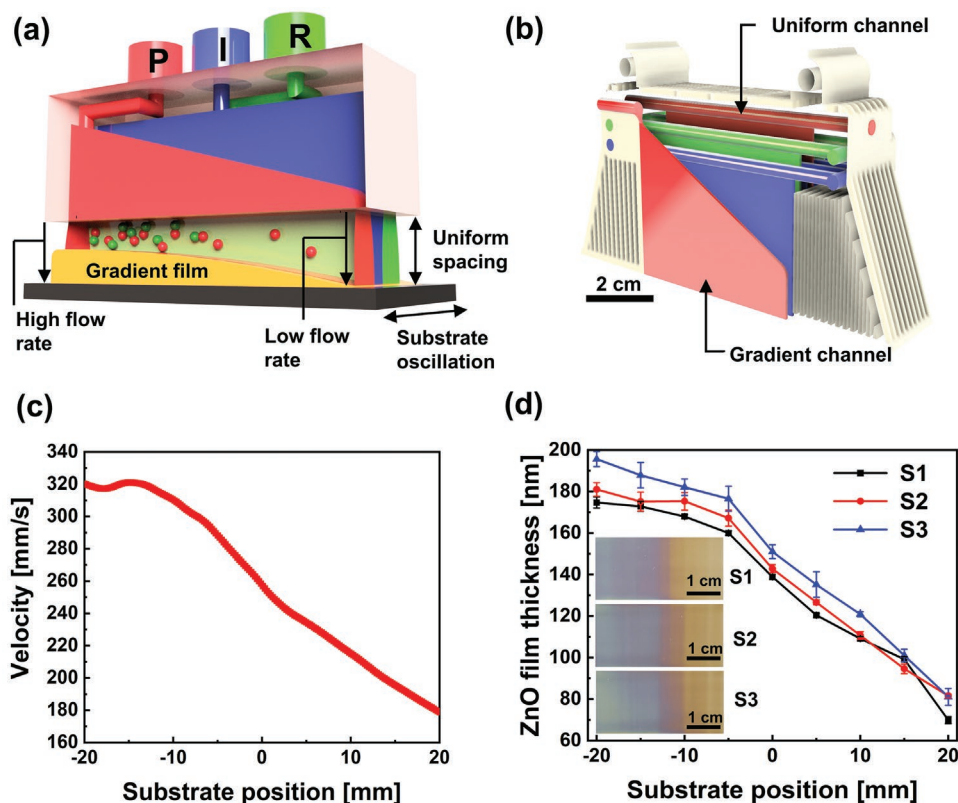


Figure 4. Deposition of gradient films with a custom-designed reactor. a) By varying the design of the precursor channel, more precursor is delivered to the left side of the substrate than the right side. If operating in AP-CVD conditions, a spatially varying deposition rate is expected. b) Design of reactor head with uniform and gradient precursor channels. The uniform channel can be used to ensure a uniform reactor-substrate spacing before switching to the gradient channel. c) CFD-simulated velocity of the gas flowing outward from the gradient channel along the substrate surface. d) Sample-to-sample variation of ZnO thickness gradient films deposited using the 3D printed custom-designed reactor. Error bars indicate the variation in film thickness perpendicular to the gradient direction.

To model the variation in precursor delivery provided by the gradient channel, we performed CFD analysis to simulate the flow of the nitrogen carrier gas through the gradient channel at normal temperature and pressure (see Figures S6 and S7 in the Supporting Information). Figure 4c shows the simulated horizontal flow outward from the channel along the substrate surface. As the velocity is proportional to the precursor flow rate, the flow variation seen in Figure 4c would be expected to result in a variation in film deposition rate when operating in AP-CVD conditions.

The optimized channel geometry was then integrated into the custom-designed reactor head and 3D printed, as shown in Figure S6 (Supporting Information). We deposited ZnO films on borosilicate glass using the custom reactor head. Figure 4d shows 3 films with thickness gradients produced using a reactor-substrate spacing of 300 μm and 175 oscillations at a speed of 30 mm s^{-1} . The film thickness was measured across the gradients using ellipsometry. A slight increase in the thickness was observed when repeating the depositions (samples S2 and S3), which is likely due to small variations in the saturation of the precursor lines. However, the 3 films have similar thickness gradients, demonstrating the good reproducibility of the custom-designed reactor. In contrast, the reproducibility of the first approach (variable reactor-substrate spacing) was limited by

the mechanical positioning of the reactor (the reactor-substrate spacing was adjusted using micrometers heads with a resolution of 20 μm). As was shown in Figure 2g, a 40 μm change in the spacing on one side of the reactor resulted in a clear change in the gradient produced. The measured thicknesses in Figure 4d indicated a GPC of 0.53 nm/cycle (0.39 nm s^{-1}) on the side with higher flow rates (left side) and 0.23 nm/cycle (0.17 nm s^{-1}) on the side with lower flow rates (right side). Notably, the variation in GPC was consistent with the simulated variation in flow velocity shown in Figure 4c.

One of the ZnO gradient films (S1) was characterized to identify any property variations across the gradient. Absorbance measurements and bandgap calculations are shown in Figure S8 in the Supporting Information. The absorbance shows a slight increase with thickness, as expected, and the bandgap remains constant at ≈ 3.4 eV, indicating minimal variation in the position of the energy levels. X-ray diffraction (XRD) was performed to investigate the growth orientation and crystallinity. Figure 5a shows that the ZnO grew in the [100], [002], [101], [102], [110], [103], and [112] directions, and that the relative height of the peaks remained similar across the gradient. The full-width-at-half-maximum (FWHM) of the 100 peaks was determined, and the crystallite size was calculated using the Scherrer equation. The FWHM has a larger value for 70–110 nm

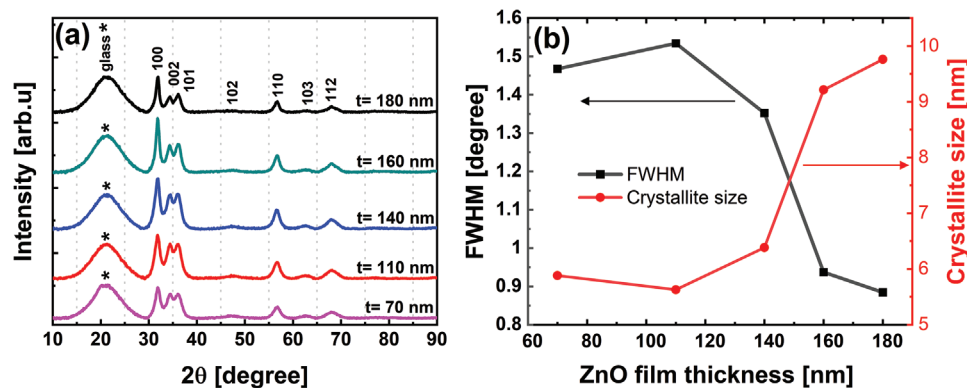


Figure 5. a) XRD measurements of the thickness gradient ZnO film S1 from Figure 4d. b) FWHM and crystallite size values measured for the 100 diffraction peaks in (a).

(Figure 5b), which may be due to mismatch strain between the ZnO film and the glass substrate, and then decreases with increasing film thickness, in agreement with Ref. [30]. As a result, the crystallite size increases with increasing film thickness.

2.2. CHT Study of Metal-Insulator-Metal Diodes

The growing “Internet of things” is pushing the integration of electronics, including electronics enabled by quantum phenomena, to a broader variety of environments. This necessitates the development of low-cost, scalable techniques for manufacturing quantum devices. MIM diodes, for example, are quantum-tunneling devices capable of rectifying high frequency alternating current (AC) to direct current (DC) via the transport of electrons through a potential barrier in femtoseconds. MIM diodes are useful in many applications including rectennas for solar harvesting,^[31] infrared detectors,^[32] and wireless power transmission.^[33] We recently demonstrated that rapid, open-air AP-CVD could be used to deposit the insulating layer for MIM diodes.^[21]

The effect of the insulator layer thickness on the performance of MIM diodes has been studied theoretically. Previous simulation work has varied the insulator thickness in the range of 0.5–2,^[34] 1–4,^[35] and 4–10 nm,^[36] along with the metal work function difference, to optimize the diode figures of merit. In contrast, few experimental studies have been performed, which is likely due to the challenging and time-consuming nature of MIM diode fabrication. Slow vacuum-based deposition methods are traditionally used to produce the required ultra-thin insulator layers. Krishnan et al.^[37] and Chin et al.^[38] examined the effect of NiO and Nb₂O₅ thickness, respectively. However, their studies were limited to only two insulator thicknesses.

In this work, we fabricated Pt/Al₂O₃/Al MIM diodes with an Al₂O₃ thickness gradient film, as illustrated in Figure 6a, to optimize the diode performance more rapidly and systematically. The variable reactor-substrate spacing approach was implemented to deposit the insulating Al₂O₃ film, with a spacing of 150 μm on one side of the reactor and 100 μm on the other. Six substrate oscillations (24 cycles) were used to deposit the gradient film. This deposition took about 45 s and

had GPCs that varied from ≈0.11 to 0.41 nm/cycle (0.05 to 0.22 nm s⁻¹) across the substrate. Aqueous sodium hydroxide was used to etch a step edge in the Al₂O₃ film before depositing the second metal (Al), in order to measure the film thickness at various locations along the substrate using atomic force microscopy (AFM). The AFM images in Figure 6f show that the Al₂O₃ thickness varied from ≈10 nm on one side to 2.5 nm on the other side of the substrate, clearly showing the ability of this technique to produce sub-10 nm thickness gradients. Finally, the top Al electrode was deposited using electron beam evaporation and lithography. There were 18 columns of diodes on the wafer such that the combinatorial approach allowed for the study of 18 different insulator thicknesses on a single substrate. Each column contained 20 diodes, enabling statistical analysis for each insulator thickness.

We performed current density–voltage (*J*–*V*) measurements on the MIM diodes to determine their figures of merit. The *J*–*V* curves were asymmetrical and nonlinear for the thicker diodes, as shown in Figure 6b for the diodes with insulator thicknesses of 8.5±1.9 and 6.5 ± 1.9 nm. In contrast, the *J*–*V* curve for a thinner insulator layer (2.5 ± 0.2 nm) in Figure 6b shows low asymmetry. We determined the turn-on voltage (TOV) by extrapolation in the linear region^[39] and it is seen to decrease from ≈3.1 to 1.0 V in Figure 6b as the insulator becomes thinner. Figure 6c–e shows the dependence of the figures of merit (asymmetry, nonlinearity, and responsivity) on the Al₂O₃ thickness. We calculated the asymmetry (ratio of forward to reverse current) at the TOV for each diode and it is seen to increase with Al₂O₃ thickness in Figure 6c, reaching a maximum value of 78 at an Al₂O₃ thickness of 6.5 nm and 1.8 V. The asymmetry decreases for insulator thicknesses larger than 6.5 nm. This is attributed to an increase in the reverse current with increasing voltage for thicker insulators, which decreases the asymmetry ratio. The nonlinearity (a measure of the degree of variation from a linear *J*–*V* curve) and responsivity (a measure of the ability of a MIM diode to generate DC current per input of AC electrical power) were calculated at the TOV and showed maximum values of 11.0 and 5.5 A W⁻¹, respectively, for an Al₂O₃ thickness of 7 nm. Therefore, this CHT study indicates that the optimum figures of merit for the Pt/Al₂O₃/Al MIM diode can be obtained with an insulator thickness of 6.5 to 7.0 nm.

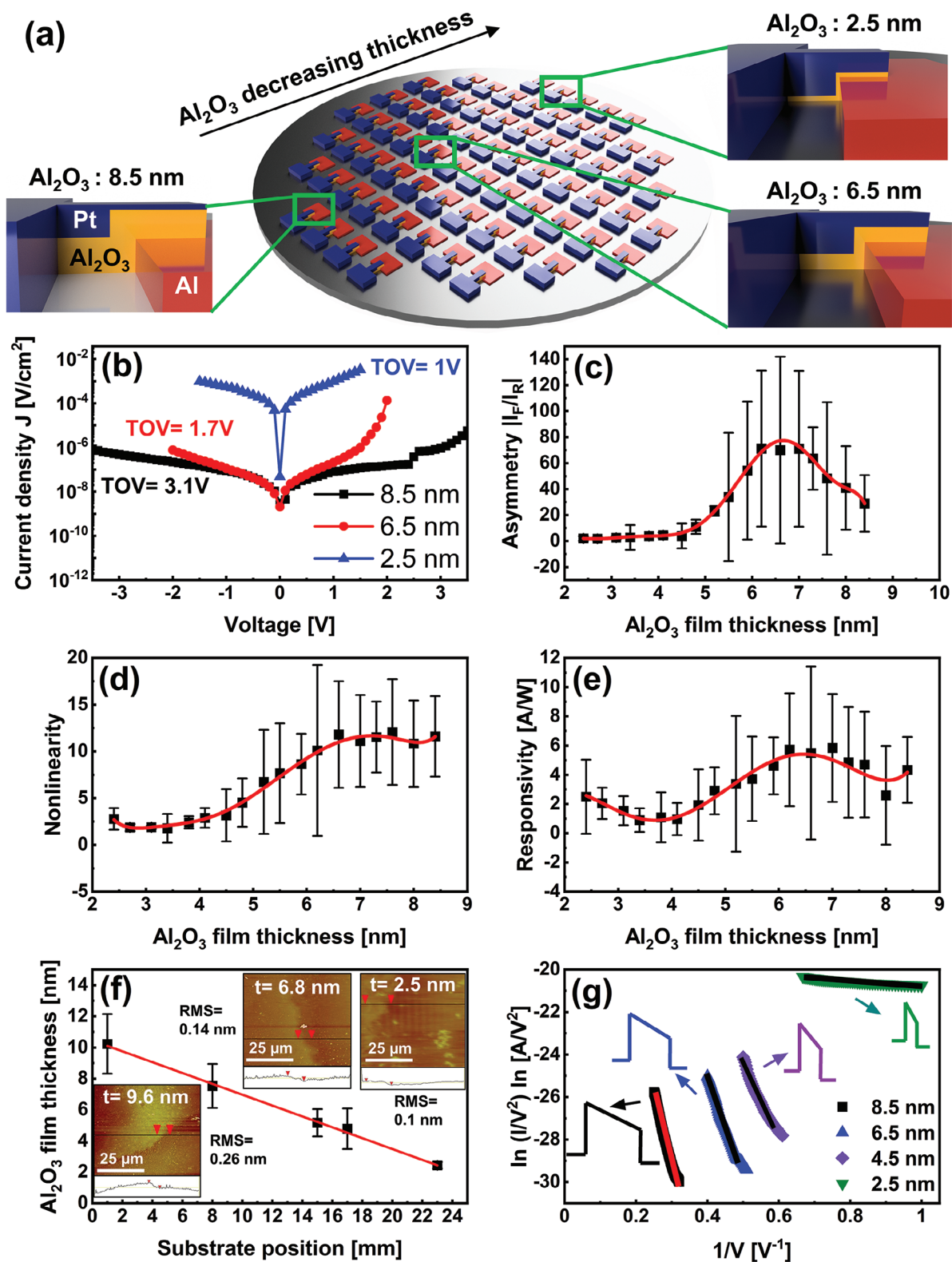


Figure 6. CHT study of MIM diodes. a) Pt/Al₂O₃/Al MIM diode architecture with Al₂O₃ thickness gradient film. Diodes with 18 different Al₂O₃ thicknesses were tested. b) J - V curves for 3 of the Pt/Al₂O₃/Al diodes. c) Asymmetry, d) nonlinearity, and e) responsivity of the diodes for the 18 different Al₂O₃ thicknesses (measured at the TOV). f) AFM measurements indicated that the Al₂O₃ film thickness varied from 10 to 2.5 nm and the RMS surface roughness increased slightly from 0.1 to 0.26 nm. g) Fowler-Nordheim tunneling plots at forward bias for Pt/Al₂O₃/Al MIM diodes with Al₂O₃ thickness gradient film. The legend indicates the Al₂O₃ thickness.

For the thin Al₂O₃ gradient films, little variation in refractive index (Figure 2h), composition (Figure 3 and Table S3: Supporting Information), and surface roughness (Figure 6f) were observed across the gradient. Therefore, it is expected that the behavior of the MIM diodes depends mostly on the thickness of the Al₂O₃. To confirm this, the *J*–*V* curves of the MIM diodes with different insulator thickness were fitted to an expected conduction mechanism, Fowler–Nordheim tunneling, as shown in Figure 6g. Figure 6g shows that as the Al₂O₃ thickness increased, the applied bias required to make Fowler–Nordheim tunneling the dominant conduction mechanism increased and the forward current was reduced, as the thicker insulator results in a reduction in the tunneling probability.

The optimized figures of merit reported here are comparable to or better than those of previously reported diodes with a single Al₂O₃ layer^[21,40–45], as summarized in Table S4 in the Supporting Information. The use of this thickness gradient Al₂O₃ film has enabled the identification of a slightly larger optimal Al₂O₃ thickness (6.5 to 7.0 nm) than what we reported previously for Pt/Al₂O₃/Al diodes deposited by AP-CVD (6 nm).^[21] The greater Al₂O₃ thickness (≈7 nm) that was identified in this CHT study does result in a lower current density compared to some of the previous reports (a decrease in current density with insulator thickness is seen in Figure 6b). Hence this thickness-dependence study experimentally demonstrates a fundamental trade-off between the figures of merit and current density (diode resistance) in Pt/Al₂O₃/Al diodes. One promising strategy to tackle this trade-off may be the use of multiple insulator layers.^[46,47] The CHT approach demonstrated here will be particularly useful for optimizing the figures of merit in diodes with multiple insulator layers.

2.3. CHT Study of Perovskite Solar Cell Thin Film Encapsulation

Organic–inorganic halide perovskite solar cells (PSCs) have attracted a great deal of attention due to their excellent absorption and charge transport properties as well as their low-cost and convenient fabrication techniques.^[48] These properties led to an incredible device power conversion efficiency improvement from 3.8% to over 25.2% in only a few years.^[49,50] However, the most challenging issue in perovskite solar cells is the long-term stability.^[51] Research indicates that the most significant source of external degradation in these cells is the decomposition of the perovskite after exposure to moisture and oxygen.^[52] External encapsulation materials (e.g., epoxies, laminated plastics) and thin film encapsulation (TFE) materials deposited directly onto the device stack are being investigated, as detailed in several excellent review articles, including some specific to ALD and CVD.^[53–55] ALD encapsulation is attractive since it provides conformal, pinhole-free barrier layers, but its slow speed hinders its practicality and prolonged heating and precursor exposure can damage the underlying layers.^[53,56] As a result, most TFE implementations have used ALD film thicknesses on the order of 20 nm or less and efforts have been made to use lower processing temperatures (e.g., 60 °C).^[53,56] However, for prototypical encapsulation films, such as Al₂O₃, lower processing temperatures have been reported to decrease the film density, increase undesirable hydroxyl content, and

increase the water vapor transmission rate (WVTR).^[57,58] In this regard, AP-SALD and AP-CVD are promising alternatives to PECVD and conventional ALD. They are capable of providing pinhole-free gas barrier layers at atmospheric pressure, and the rapid nature of AP-SALD and AP-CVD (can be more than 100 times faster than conventional ALD) limits the required heating time of the perovskite and potential damage. It has been shown that TiO₂, SnO_x, and CuO_x charge-transport layers can be deposited on top of perovskite films by AP-SALD/AP-CVD at temperatures as high as 180 °C.^[59,60] Hence, the higher deposition rate of AP-SALD and AP-CVD enables a larger TFE processing window (temperature and thickness range) to be explored for PSCs.

We demonstrate AP-CVD of an Al₂O₃ TFE, which is a prototypical TFE material,^[53,54,57,61] on top of a perovskite solar cell stack for the first time. Spatial ALD Al₂O₃ has been reported to have a WVTR on the order of 10^{–6} g m^{–2} d^{–1} at room temperature.^[45] A gradient film of Al₂O₃, was used to study TFE thicknesses up to 70 nm, a larger range than has typically been tested with conventional ALD. Thicker Al₂O₃ layers may be expected to provide better encapsulation; however, practical considerations (deposition time and cost) favor thinner layers for commercialization. Furthermore, it has been demonstrated for ALD films that the improvement in barrier properties with thickness can be sub-linear^[62,63] and can show low thickness dependence^[64]. Klumbies et al.^[62] showed fast degradation for devices encapsulated with 100 nm of Al₂O₃ because of the formation of the large cracks resulting from increased film stress with thicker films^[62,65]. Hence thickness-dependent studies are essential to identify optimal thicknesses. PSCs often display significant performance variability, and our approach allows the influence of the TFE thickness to be studied in a single device, avoiding batch-to-batch comparisons. We used the variable reactor-substrate spacing method to deposit an Al₂O₃ film with a thickness gradient (70–40 nm) as an encapsulation layer on top of a 5 × 5 cm formamidinium-cesium lead iodide PSC. 60 substrate oscillations (120 cycles) and a spacing of 200–100 μm were used to deposit the gradient film. The deposition took only 5 min, such that no degradation of the perovskite was observed when heating the device to 130 °C for the deposition. The perovskite solar cell architecture is shown in Figure 7a and consisted of glass/FTO/TiO₂ (55 nm)/perovskite (315 nm)/Spiro-OMeTAD (370 nm)/Al₂O₃ (70–40 nm). The top metal electrode was omitted to avoid known issues with iodine migration to the metal electrode^[66] and to facilitate the absorbance as well as the neural network characterization discussed hereafter.

To study the effect of the larger Al₂O₃ TFE thickness on perovskite stability, we placed PSCs with and without the Al₂O₃ TFE in a humidity chamber with 60% RH at room temperature. The absorbance of the PSC was measured at different positions across the device (corresponding to different TFE thicknesses) after various durations in the humidity chamber. Figure 7b,c shows the absorbance versus H₂O exposure time at wavelengths of 500 and 630 nm, respectively. A clear trend is seen after 25 h, where the absorbance drops more significantly for locations where the TFE is thinner, indicating more perovskite degradation. The reduction in absorbance (and hence degradation of the perovskite) is greatest for the device with no Al₂O₃ TFE. The photoluminescence (PL) of the PSC (excitation

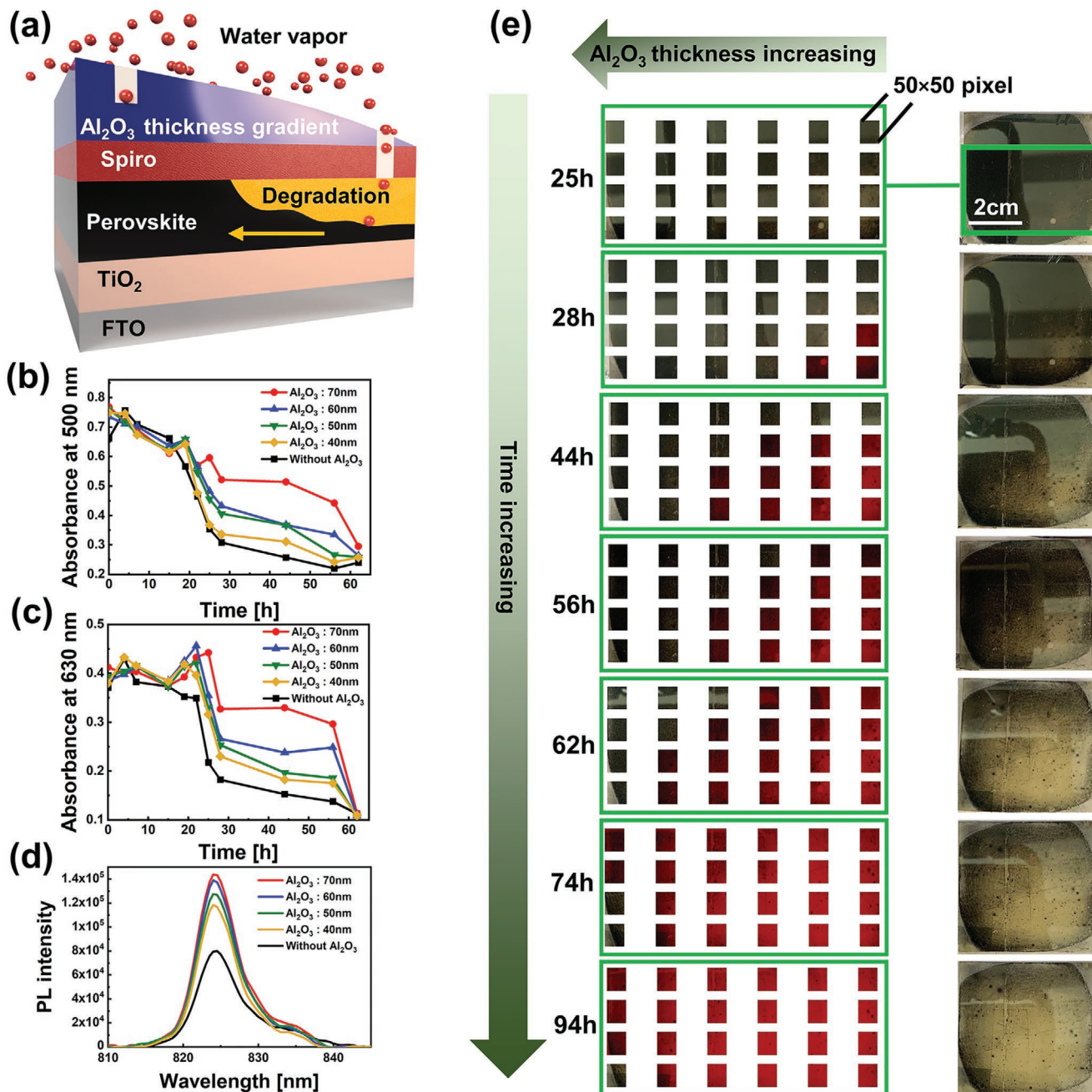


Figure 7. CHT study of perovskite solar cell thin film encapsulation. a) Perovskite solar cell architecture with Al_2O_3 gradient TFE. b,c) Plots of PSC absorbance versus time at different positions across the PSC (corresponding to different TFE thicknesses) and for a PSC with no TFE at wavelengths of 500 and 630 nm. d) PL spectra of the PSCs at 28 h. e) Spatially resolved classification of the PSC degradation by a convolutional neural network. Red coloration indicates perovskite degradation. The onset of PSC degradation is observed to occur at different times for different TFE thicknesses.

at 680 nm) was also measured after 28 h at various locations across the device with the Al_2O_3 thickness gradient TFE and for the device without a TFE, as shown in Figure 7d. As expected, the PL measurements show that the PL intensity of the perovskite peak at 825 nm decreases with decreasing Al_2O_3 TFE thickness, indicating that the perovskite degrades faster when the TFE is thinner. This is consistent with a previous study of ALD Al_2O_3 barrier films for OLEDs.^[62] The smaller peak at 835 nm is attributed to the TiO_2 film^[67,68] in the device stack.

For CHT study of the PSCs, we developed a simple convolutional neural network (CNN) to determine the effectiveness of the Al_2O_3 TFE, the architecture of which can be seen in Figure S9 in the Supporting Information. CNNs have been used to perform many image processing tasks in materials science, such as detecting 2D materials in microscope images,^[69] improving X-ray diffraction test speed,^[70] and predicting chemical properties.^[71] CNNs are designed to mimic the human eye in function, recognizing how colors, shapes, and edges build

to form a complete picture,^[72] which makes them robust to changes in lighting or image orientation when well trained. In our work, the effectiveness of the TFE is directly correlated with the rate of decay of the perovskite layer. As per Figure 7a, as the perovskite reacts with water, lead iodide is formed, turning the perovskite from black to translucent yellow. In this case, the CNN need only to identify the color of the input image, and identify any abrupt edges, such as cracks or holes in the film in order to classify the image as either “degraded”, “intact”, or “no film” present.

Images of the PSCs were taken at various intervals, from various angles and under different light conditions over the ≈ 100 h it took for the films to degrade in the humidity chamber. These were then subdivided into smaller 50×50 -pixel images, as can be seen in Figure 7e, which serve as the input to the CNN. This subdivision serves three purposes, firstly it boosts the training data size by several orders of magnitude, secondly it simplifies each input sample so a smaller and faster CNN can be used, and thirdly it spatially resolves the degradation of the perovskite layer. It is the third advantage that allows us to compare and evaluate the various Al_2O_3 TFE thicknesses. The colors are coded according to the three possible predictions provided by the Neural Network. A red overlay is placed on a 50×50 -pixel image if the probability that the sub-section is degraded is greater than the other two possibilities (there is no correlation to the degree of degradation). In Figure 7e, the Al_2O_3 TFE thickness increases from right to left. After 25 h H_2O exposure time, a clear hole appeared in the area with thinner Al_2O_3 , indicating that water had penetrated through the TFE and Spiro-OMeTAD into the perovskite layer. After 28 h the CNN identified that the perovskite started to degrade wherever the Al_2O_3 was thinnest, as indicated by the red coloration in the pixelated images. This is consistent with the lower absorbances and PL intensity for Al_2O_3 ;40 nm in Figure 7b–d. The degradation, which is indicated in red, progresses from parts of the device with thinner TFE to thicker TFE with increasing H_2O exposure time, as shown from 28 to 94 h. The insets in Figure 7e shows the PSC at different H_2O exposure times. It is seen that the degradation begins earlier for the bottom row of pixels than the top row. This is attributed to the presence of some thickness variation in the perpendicular direction, which was shown in Figure 2g. The thickness gradient across the top of the sample appears to be slightly thicker than the gradient across the bottom.

The superior performance of the thicker TFE suggests that the thicker AP-CVD Al_2O_3 maintains its compactness and is free of stress-induced cracking^[62], at least up to the 70 nm thickness examined here. This is consistent with the uniform refractive index (1.78–1.8) measured for the 70–40 nm thickness range (Figure S5, Supporting Information), as well as microscope images of a 75–45 nm Al_2O_3 thickness gradient film in Figure S10 (Supporting Information), which showed no cracks for thicknesses up to 75 nm. In contrast, the micrographs indicated the presence of some film regions with pinholes at the 45 nm gradient thickness and to a lesser extent at 55 nm, consistent with the faster degradation observed.

Table S5 in the Supporting Information details some previous AlO_x TFE studies for PSCs^[56,57,73–75], including the deposition time, temperature, TFE thickness, and degradation time. While these studies reported longer degradation times for similar

humidity conditions to those examined here, they make use of conventional ALD to deposit the TFE. As shown in Table S5 (Supporting Information), the deposition rates and deposition times (e.g., >100 min) associated with ALD are impractical for manufacturing TFE for PSCs. Here we have demonstrated AP-CVD of an Al_2O_3 TFE, on top of a PSC stack for the first time. While stability optimization of the AP-CVD Al_2O_3 films is needed in the future, the short deposition time (5 min) avoids damage to the perovskite layer and is compatible with large-scale manufacturing.

These nanoscale film thickness gradients will provide a useful platform to further optimize the thicker TFE layers that are practical with AP-SALD/CVD. Al_2O_3 has also been a key component in TFEs based on oxide^[61] and organic–inorganic^[54,57,76] multilayers/nanolaminates. The gradient films will be particularly useful for optimizing the thicknesses of multiple oxide films simultaneously, although the complexity, cost, and industrial practicality of the nanolaminate films should be kept in mind.

3. Conclusion

In this work, we produced thin films with nanoscale thickness gradients in open-air by spatially varying the CVD rate across a substrate. We deposited ZnO and Al_2O_3 films with nm-scale thickness gradients (including sub-10 nm films) in as little as 45 s. The GPCs were observed to vary from as little as 0.23 nm/cycle to as much as 1.2 nm/cycle across the substrate, providing precise control over film thickness at different substrate locations. The achievable GPC range can be increased in the future and the techniques can be applied to deposit a range of semiconductors, insulators, and metals that are compatible with similar ALD and CVD methods.

We used rapidly printed Al_2O_3 films with thickness gradients to perform CHT studies of quantum-tunneling MIM diodes and PSC encapsulation. In the case of the MIM diodes, an Al_2O_3 film with thickness varying from 10 to 2.5 nm was used to test 360 diodes with 18 different insulator thicknesses on a single substrate. No other open-air technique currently exists to produce a sub-10 nm gradient Al_2O_3 film such as this, and this work represents a significant advancement compared to previous studies that examined a limited number of insulator thicknesses. To our knowledge, more Al_2O_3 thickness-dependence data is obtained from this single CHT wafer than all previous experimental reports combined. The diode figures of merit were strongly influenced by the Al_2O_3 thickness and the best diode performance was found for a larger thickness than reported previously (6.5 to 7 nm), for which the asymmetry, nonlinearity, and responsivity were 78, 11, and 5.5 A W^{-1} respectively. This CHT study also experimentally highlights the fundamental trade-off between the figures of merit and diode resistance in a Pt/ Al_2O_3 /Al diode.

In the second example, an Al_2O_3 encapsulation film was deposited by AP-CVD on a PSC stack for the first time. A 70–40 nm thickness gradient was employed on top of a 5×5 cm PSC. Deposition of these thicknesses would be prohibitively slow with conventional ALD. In contrast, AP-CVD is roll-to-roll compatible and the rapid nature of the spatially varying CVD

technique enabled deposition of the TFE without causing degradation of the underlying perovskite film. The degradation timescale of the PSC in a humid environment, as characterized by spatially resolved absorbance and PL measurements, was observed for multiple TFE thicknesses on a single substrate. A high-throughput method using CNNs was also developed to analyze the Al₂O₃ TFE, which identified the areas of the perovskite that had degraded, and therefore the efficacy of the protective layer. By constantly analyzing the visual characteristics of the film, the point at which the film degrades was identified at various locations on the device. Compared to conventional methods, this CNN method requires no special equipment and can be used for combinatorial study of multiple films and their effect on the perovskite layer. While it does not identify specific degradation mechanisms, it can continuously monitor the film and therefore provide excellent spatial and temporal information about the degradation. From this CHT study it can be concluded that Al₂O₃ TFEs deposited by rapid, open-air AP-CVD slow water-induced degradation, and that the effectiveness of the TFE increases with thickness, at least up to 70 nm, as no stress-induced film cracking was observed. Thicker Al₂O₃ TFEs, both single and multilayer, can be optimized in the future, but the impact of a longer TFE deposition on the cost and perovskite stability would need to be considered.

The nanoscale thickness gradient films introduced in this work can be used to optimize different device architectures (e.g., metal-insulator-insulator-metal diodes, different perovskite materials and TFEs) and measure different device properties (e.g., TFE water vapor transmission rates) in the future. More generally, the nanoscale film thickness gradients can be used for CHT studies of a wide range of devices, such as solar cells, LEDs, flexible electronics, and batteries, among others.

4. Experimental Section

AP-CVD Film Deposition: For all depositions, the reactor-substrate spacing was adjusted using micrometer heads with a resolution of 20 μm. For the deposition of ZnO films using the variable reactor-substrate spacing method, N₂ was bubbled through the DEZ precursor at 15 sccm and combined with an 85 sccm N₂ carrier gas. The H₂O was bubbled at 30 sccm and combined with a 170 sccm N₂ carrier flow. The resulting flow per outlet channel was 100 sccm. A 600 sccm flow of N₂ inert gas was used to partially separate the precursors and remove excess unreacted precursors or reaction by-products. The substrate was heated to 150 °C. For the deposition of ZnO films using the custom-designed reactor head, N₂ was bubbled through the DEZ at 25 sccm and combined with a 75 sccm N₂ carrier flow. The H₂O was bubbled at 32 sccm and combined with a 298 sccm N₂ carrier flow. The resulting flow per outlet channel was 100 sccm for the 1 gradient precursor channel and 110 sccm for the 3 reactant channels. A 660 sccm flow of N₂ inert gas was used, resulting in a flow per channel of 94 sccm (6 inert curtain channels and 1 uniform channel). The substrate was heated to 100 °C and oscillated at a speed of 30 mm s⁻¹. For the deposition of Al₂O₃ gradient films on the Si substrate and the MIM diodes, N₂ was bubbled through the TMA precursor at 15 sccm and combined with a 235 sccm N₂ carrier gas. The H₂O was bubbled at 100 sccm and combined with a 275 sccm N₂ carrier flow. The resulting flow per outlet channel was 125 sccm. A 750 sccm flow of N₂ inert gas was used. The substrate was heated to 150 °C. For the deposition of Al₂O₃ films for PSCs, both TMA and DEZ precursors were employed. The DEZ was bubbled throughout the deposition to facilitate film nucleation at a lower

substrate temperature of 130 °C, to prevent damage to the perovskite film. N₂ was bubbled through the TMA and DEZ precursors at 38 and 10 sccm, respectively, and combined with a 235 sccm N₂ carrier gas. The H₂O and N₂ inert gas flows were the same as for the Al₂O₃ deposited for the MIM diodes.

Film Thickness Measurements: A Woollam M-2000 DI ellipsometer with a wavelength range of 200–1800 nm was used to measure the thicknesses and refractive indices of ZnO and Al₂O₃ films, which were modeled using the Cauchy formula.

Atomic Force Microscopy: A dimension 3100 atomic force microscope (AFM) was used to measure the film thickness and roughness.

UV-Vis Absorption Spectroscopy for PSC: The samples were placed inside a humidity chamber and moved to measure different locations on the surface of the samples. An Ocean Optics DH-2000 lamp was used as a light source and an Ocean Optics HDX spectrometer was used to measure the transmitted light.

Photoluminescence Spectroscopy for PSC: A Quanta Master 8000 Fluorometer by HORIBA was used to perform PL on PSCs by exciting at 680 nm in a spectral range of 810 to 850 nm. The sample was moved to different locations for measurements.

X-Ray Diffraction: XRD measurements of ZnO films that were deposited on glass substrates were performed by a XPERT-PRO diffractometer with Cu Kα radiation (X-ray wavelength 0.154 nm).

X-Ray Photoelectron Spectroscopy: A VG Scientific ESCALAB 250 system was used to examine the surface of the films using Al Kα X-rays.

Optical Microscopy: Optical microscope images of an Al₂O₃ thickness gradient film were obtained with an OLYMPUS MX61A optical microscope.

CFD Simulation: All meshing and simulations were performed using ANSYS CFX. The CFD model uses hexahedral cells throughout the structured mesh to preserve flow physics and to reduce inherent numerical errors in the analysis which are common when using a tetrahedral mesh. The mesh was constructed based on a y+ value of 1, where the first layer height is 0.045 mm, and at least 15 cell layers are maintained in the buffer layer (y+ below 30) as shown in Figure S5 in the Supporting Information. The SST model was used, which solves the near wall viscous effects numerically, preserving the simulated flow as much as possible without presuming or forcing the flow to be in the turbulent regime. The simulation uses an inlet mass flow rate of 2 × 10⁻⁶ kg s⁻¹ which translates to ≈100 sccm based on the inlet area. A symmetry boundary condition along the midplane of the channel was used to reduce computational resources. High-resolution advection and turbulence schemes were chosen for a more accurate result. MAX iteration residuals of 1 × 10⁻⁴ was used as the results did not vary much compared to MAX residuals of 1 × 10⁻⁵. A grid convergence study was also performed on the mesh and found that the grid converged at 4× grid refinement, from 31 668 to 126 600 elements. A total of 89 and 133 iterations were needed for the simulations to converge for the laminar and SST cases, respectively.

Design and 3D Printing of the Reactor Head: The reactor head was designed using Siemens NX. The design was 3D printed using Form 2, a stereolithography (SLA) based 3D printer by Formlabs. The SLA 3D printing process builds the part layer by layer using a 140 μm laser source in the XY-direction to cure solid parts from a liquid photopolymer resin as the part moves in the Z-direction. High Temp V2 resin from Formlabs was used for the print since the cured resin provides a high heat deflection temperature of 142 °C according to its datasheet. The print layer thickness resolution was set to 50 μm. In addition to standard washing of the printed reactor in a sonicated isopropanol bath (Form Wash by Formlabs), a blade and an air compressor gun was used to scrape and blow the excess uncured resin out from the channels, respectively. Isopropanol was also injected through each channel at least 3 times to thoroughly clean and flush out residual resin that may be stuck in the channels. The cleaned reactor was then cured by exposing it to UV light in Form Cure by Formlabs at 70 °C for 120 min. A lower curing temperature of 70 °C was decided to be used as opposed to the recommended 80 °C to prevent warpage of the reactor that was observed on previous iterations.

MIM Diode Fabrication: The diodes were produced on a 3 in. SiO₂ wafer. A layer of negative photoresist maN-1410 was spin-coated onto the wafer. The photoresist was then patterned using a mask aligner to pattern the first electrode with device areas measuring 100 μm². After that, the sample was developed in Ma-D 533/S. The bottom Pt electrodes with 100 nm thickness were deposited using an E-beam evaporation system with a base pressure set to 4 × 10⁻⁶ Torr and a 1 Å s⁻¹ deposition rate. The photoresist was lifted off, forming the bottom Pt electrode of the MIM diode. A thickness gradient film of Al₂O₃ was then deposited as described above. To deposit the Al top contact of the MIM diode, a process similar to that used to deposit the bottom contact was used. The bottom Al contact on the sample was aligned with another mask and photoresist was exposed. Reactive ion etching was used to remove any oxidant on top of the electrodes.

Perovskite Solar Cell Fabrication: Fluorine doped tin oxide (FTO) glass substrates (5 × 5 cm) were washed in a 2% aqueous extran 300 detergent, deionized water, and 2-propanol (20 min each), then, dried using a hotplate at 150 °C for 0.5 h, after which they were allowed to cool. A titanium dioxide (TiO₂) layer was prepared by dissolving a 0.1 M solution of titanium diisopropoxide bis(acetylacetonate) in 1-butanol and then spin coating three times at 4000 rpm for 10 s in a fume hood. In between each spin-coating, the samples were annealed at 125 °C for 5–10 min then allowed them to cool down for 1 min. Organic residues were eliminated by increasing the temperature (from 125 to 450 °C), holding at 450 °C for 0.5 h, and then decreasing the temperature from 450 °C to room temperature, using ramp rates of ≈15 °C min⁻¹. The perovskite layer was made by preparing an anhydrous stock solution of 1.4 M PbI₂, 1.25 M formamidinium iodide (FAI), 0.0987 M CsI, and 0.0833 M GAI in 76:24 ratio v/v in DMF/DMSO solvent in a nitrogen glovebox. Then, it was passed through a 0.45 μm polytetrafluoroethylene syringe filter and stirred for 30 min. The solution was deposited on the substrates by spin-coating at 1000 rpm for 10 s followed by 6000 rpm for 20 s in the glovebox. In the last 5 s of spin-coating, 200 μL of a 50/50 v/v anhydrous solution of chlorobenzene and chloroform was dispensed as an antisolvent. Immediately after spinning, the samples were annealed at 140 °C for about 0.5 h in the glovebox and allowed to slowly cool down to room temperature. For the hole transport layer, a solution of 70.0 × 10⁻³ M Spiro-OMeTAD was prepared in chlorobenzene in the glovebox by adding 18 μL of 4-*tert*-butyl pyridine and chlorobenzene (60:40 v/v) and 18 μL of a 1.0 M Li-TFSI solution in acetonitrile to 1000 μL of the Spiro-OMeTAD solution. After filtering the solution through a 0.45 μm polytetrafluoroethylene syringe filter, it was spin-coated at 4000 rpm for 15 s. Lastly the Al₂O₃ thickness gradient film was deposited on top of the Spiro-OMeTAD layer, as described above.

Convolutional Neural Network: Over 5,000 50 × 50-pixel sub-images were labelled and used to train the CNN, combining samples with intact and degraded films, as well as some where no film was present. The CNN was created using MATLAB's Deep Network Designer and trained using stochastic gradient descent with a learning rate of 0.01. Due to the relatively small set of training data, the size of the network was kept to a minimum, trading prediction accuracy for a reduced risk of overfitting and faster computation time. A network with three blocks of convolution, batch normalization and ReLU (Rectified Linear Unit) layers separated by max pooling layers was found to strike the best balance between efficiency and accuracy. For training the network, 20% of the images were reserved for later testing, and the remaining images were split 80% training and 20% validation, with the images in each set shuffled after every training epoch to minimize overfitting. At the output layer, a Softmax activation function provides the relative probabilities of the sub-image belonging to each of the three classes (see Figure S9 in the Supporting Information). Using the 20% of the samples that were reserved for testing, the CNN was able to predict the class to which the sub-image belonged with 89.9% accuracy. Each Perovskite solar cell image takes less than a second to pass through the CNN, meaning that this method can be applied to video data, providing real-time data on the status of the solar cell. The ability to constantly monitor the cells will offset any loss of accuracy using this method compared to more detailed absorbance measurements which cannot be performed as

frequently and often require exposing the solar cell to an uncontrolled environment.

Supporting Information

Supporting Information is available from the Wiley Online Library or from the author.

Acknowledgements

V.H.N. and A.J. contributed equally to this work. A.H.A. would like to acknowledge Prince Sattam bin Abdulaziz University, Alkharj, Saudi Arabia, for financial support. D.M.-R. acknowledges support from the European Union's Horizon 2020 FETOPEN-1-2016-2017 research and innovation program under Grant Agreement 801464 and through the Marie Curie Actions (FP7/2007-2013, Grant Agreement No. 63111). The Agence Nationale de la Recherche (ANR, France) is also acknowledged for funding via the programs ANR-16-CE05-0021 (DESPATCH). V.H.N. acknowledges a PhD grant from "ARC Energies Auvergne-Rhône Alpes". This project was also financially supported by "Carnot Energies du Futur" (ALDASH project). K.P.M. acknowledges funding from the NSERC Discovery Program (RGPIN-2017-04212, RGPAS-2017-507977), Canada Foundation for Innovation John R. Evans Leaders Fund (Project 35552), Ontario Research Fund – Research Infrastructure (Project 35552), and Ontario Ministry of Colleges and Universities Early Researcher Award (ER18-14-263). K.P.M. acknowledges S. Yareusevych for helpful discussions.

Conflict of Interest

The authors declare no conflict of interest.

Data Availability Statement

Research data are not shared.

Keywords

chemical vapor deposition, high throughput techniques, MIM diodes, perovskite solar cells, thickness gradient

Received: April 6, 2021
Published online: June 10, 2021

- [1] H. Koinuma, I. Takeuchi, *Nat. Mater.* **2004**, *3*, 429.
- [2] A. M. Saranya, A. Morata, D. Pla, M. Burriel, F. Chiabrera, I. Garbayo, A. Hornés, J. A. Kilner, A. Tarancón, *Chem. Mater.* **2018**, *30*, 5621.
- [3] M. Reinke, Y. Kuzminykh, P. Hoffmann, *Chem. Mater.* **2015**, *27*, 1604.
- [4] W. Lei, L. Henn-Lecordier, M. Anderle, G. W. Rubloff, M. Barozzi, M. Bersani, *J. Vac. Sci. Technol., B: Microelectron. Nanometer Struct. Process., Meas., Phenom.* **2006**, *24*, 780.
- [5] H. Salami, A. Poissant, R. A. Adomaitis, *J. Vac. Sci. Technol., A* **2017**, *35*, 01B101.
- [6] Y. W. Lai, M. Krause, A. Savan, S. Thienhaus, N. Koukourakis, M. R. Hofmann, A. Ludwig, *Sci. Technol. Adv. Mater.* **2011**, *12*, 054201.

- [7] H. Oguchi, J. Hatrick-Simpers, I. Takeuchi, E. J. Heilweil, L. A. Bendersky, *Rev. Sci. Instrum.* **2009**, *80*, 073707.
- [8] A. Kafizas, G. Hyett, I. P. Parkin, *J. Mater. Chem.* **2009**, *9*, 1399.
- [9] M. Pavan, S. Rühle, A. Ginsburg, D. A. Keller, H. N. Barad, P. M. Sberna, D. Nunes, R. Martins, A. Y. Anderson, A. Zaban, E. Fortunato, *Sol. Energy Mater. Sol. Cells* **2015**, *132*, 549.
- [10] C. M. Stafford, K. E. Roskov, T. H. Epps, M. J. Fasolka, *Rev. Sci. Instrum.* **2006**, *77*, 023908.
- [11] R. L. Davis, S. Jayaraman, P. M. Chaikin, R. A. Register, *Langmuir* **2014**, *30*, 5637.
- [12] S. Klinkhammer, X. Liu, K. Huska, Y. Shen, S. Vanderheiden, S. Valouch, C. Vannahme, S. Bräse, T. Mappes, U. Lemmer, *Opt. Express* **2012**, *20*, 6357.
- [13] A. Kafizas, C. Crick, I. P. Parkin, *J. Photochem. Photobiol., A* **2010**, *216*, 156.
- [14] Dedova, *Ph.D. Thesis*, Tallinn University of Technology, **2007**.
- [15] V. H. Nguyen, J. Resende, C. Jiménez, J. L. Deschanvres, P. Carroy, D. Muñoz, D. Bellet, D. Muñoz-Rojas, *J. Renewable Sustainable Energy* **2017**, *9*, 021203.
- [16] P. Poodt, D. C. Cameron, E. Dickey, S. M. George, V. Kuznetsov, G. N. Parsons, F. Roozeboom, G. Sundaram, A. Vermeer, *J. Vac. Sci. Technol., A* **2012**, *30*, 010802.
- [17] K. P. Musselman, C. F. Uzoma, M. S. Miller, *Chem. Mater.* **2016**, *28*, 8443.
- [18] D. Muñoz-Rojas, V. Huong Nguyen, C. Masse de la Huerta, C. Jiménez, D. Bellet, in *Chemical Vapor Deposition for Nanotechnology* (Ed: P. Mandracci), IntechOpen, London, UK **2019**.
- [19] Alshehri, *Master thesis*, University of Waterloo, **2017**.
- [20] C. M. de la Huerta, V. H. Nguyen, J. M. Dedulle, D. Bellet, C. Jiménez, D. Muñoz-Rojas, *Coatings* **2019**, *9*, 5.
- [21] A. H. Alshehri, K. Mistry, V. H. Nguyen, K. H. Ibrahim, D. Muñoz-Rojas, M. Yavuz, K. P. Musselman, *Adv. Funct. Mater.* **2019**, *29*, 1805533.
- [22] K. P. Musselman, D. Muñoz-Rojas, R. L. Z. Hoye, H. Sun, S. L. Sahonta, E. Croft, M. L. Böhm, C. Ducati, J. L. MacManus-Driscoll, *Nanoscale Horiz.* **2017**, *2*, 110.
- [23] V. H. Nguyen, A. Sekkat, C. A. Masse de la Huerta, F. Zoubian, C. Crivello, J. Rubio-Zuazo, M. Jaffal, M. Bonvalot, C. Vallée, O. Aubry, H. Rabat, D. Hong, D. Muñoz-Rojas, *Chem. Mater.* **2020**, *32*, 5153.
- [24] K. Mistry, A. Jones, M. Kao, T. W.-K. Yeow, M. Yavuz, K. P. Musselman, *Nano Express* **2020**, *1*, 010045.
- [25] C. Barbos, D. Blanc-Pelissier, A. Fave, E. Blanquet, A. Crisci, E. Fourmond, D. Albertini, A. Sabac, K. Ayadi, P. Girard, M. Lemiti, *Energy Procedia* **2015**, *77*, 558.
- [26] A. H. Alshehri, N. Nelson-Fitzpatrick, K. H. Ibrahim, K. Mistry, M. Yavuz, K. P. Musselman, *J. Vac. Sci. Technol., A* **2018**, *36*, 031602.
- [27] Y. Zhang, M. Creatore, Q. B. Ma, A. El Boukili, L. Gao, M. A. Verheijen, M. W. G. M. T. Verhoeven, E. J. M. Hensen, *Appl. Surf. Sci.* **2015**, *330*, 476.
- [28] K. B. Jinesh, J. L. van Hemmen, M. C. M. van de Sanden, F. Roozeboom, J. H. Klootwijk, W. F. A. Besling, W. M. M. Kessels, *J. Electrochem. Soc.* **2011**, *158*, G21.
- [29] C. A. M. de la Huerta, V. H. Nguyen, A. Sekkat, C. Crivello, F. Toldra-Reig, P. Veiga, C. Jimenez, S. Quessada, C. Jimenez, D. Muñoz-Rojas, *Adv. Mater. Technol.* **2020**, *5*, 2000657.
- [30] J. M. Myoung, W. H. Yoon, D. H. Lee, I. Yun, S. H. Bae, S. Y. Lee, *Jpn. J. Appl. Phys., Part 1* **2002**, *41*, 28.
- [31] E. Donchev, J. S. Pang, P. M. Gammon, A. Centeno, F. Xie, P. K. Petrov, J. D. Breeze, M. P. Ryan, D. J. Riley, N. M. Alford, *MRS Energy Sustainability* **2014**, *1*, E1.
- [32] M. N. Gadalla, M. Abdel-Rahman, A. Shamim, *Sci. Rep.* **2014**, *4*, 4270.
- [33] K. Bhatt, C. C. Tripathi, *Indian J. Pure Appl. Phys.* **2015**, *53*, 827.
- [34] S. Grover, G. Moddel, in *Rectenna Solar Cells*, Springer, New York, USA **2013**.
- [35] I. E. Hashem, N. H. Rafat, E. A. Soliman, *IEEE J. Quantum Electron.* **2013**, *49*, 72.
- [36] K. Mistry, M. Yavuz, K. P. Musselman, *J. Appl. Phys.* **2017**, *121*, 184504.
- [37] S. Krishnan, E. Stefanakos, S. Bhansali, *Thin Solid Films* **2008**, *516*, 2244.
- [38] M. L. Chin, P. Periasamy, T. P. O'Regan, M. Amani, C. Tan, R. P. O'Hayre, J. J. Berry, R. M. Osgood, P. A. Parilla, D. S. Ginley, M. Dubey, *J. Vac. Sci. Technol., B* **2013**, *31*, 051204.
- [39] A. Ortiz-Conde, F. J. García Sánchez, J. J. Liou, A. Cerdeira, M. Estrada, Y. Yue, *Microelectron. Reliab.* **2002**, *42*, 583.
- [40] E. C. Kinzel, R. L. Brown, J. C. Ginn, B. A. Lail, B. A. Slovick, G. D. Boreman, *Microwave Opt. Technol. Lett.* **2013**, *55*, 489.
- [41] J. A. Bean, B. Tiwari, G. H. Bernstein, P. Fay, W. Porod, *J. Vac. Sci. Technol., B: Microelectron. Nanometer Struct. Process., Meas., Phenom.* **2009**, *27*, 11.
- [42] B. Tiwari, J. A. Bean, G. Szakmány, G. H. Bernstein, P. Fay, W. Porod, *J. Vac. Sci. Technol., B: Microelectron. Nanometer Struct. Process., Meas., Phenom.* **2009**, *27*, 2153.
- [43] P. Periasamy, H. L. Guthrey, A. I. Abdulgatov, P. F. Ndione, J. J. Berry, D. S. Ginley, S. M. George, P. A. Parilla, R. P. O'Hayre, *Adv. Mater.* **2013**, *25*, 1301.
- [44] A. Yahyaoui, A. Elsharabasy, J. Yousaf, H. Rmili, *Sensors* **2020**, *20*, 7023.
- [45] K. Bhatt, S. Kumar, C. C. Tripathi, *AEU – Int. J. Electron. Commun.* **2019**, *111*, 152925.
- [46] F. Aydinoglu, M. Alhazmi, B. Cui, O. M. Ramahi, M. Irannejad, M. Yavuz, *Austin J. Nanomed. Nanotechnol.* **2013**, *1*, 3.
- [47] A. Y. Elsharabasy, A. H. Alshehri, M. H. Bakr, M. J. Deen, K. P. Musselman, M. Yavuz, *AIP Adv.* **2019**, *9*, 115207.
- [48] M. A. Green, A. Ho-Baillie, H. J. Snaith, *Nat. Photonics* **2014**, *8*, 506.
- [49] W. S. Yang, B. W. Park, E. H. Jung, N. J. Jeon, Y. C. Kim, D. U. Lee, S. S. Shin, J. Seo, E. K. Kim, J. H. Noh, S. Il Seok, *Science* **2017**, *356*, 1376.
- [50] NREL, Best Research-Cell Efficiencies Chart, www.nrel.gov/pv/assets/images/efficiency-chart.png (accessed: September, **2020**).
- [51] D. Zhou, T. Zhou, Y. Tian, X. Zhu, Y. Tu, *J. Nanomater.* **2018**, *2018*, 81480792.
- [52] N. G. Park, *J. Phys. Chem. Lett.* **2013**, *4*, 2423.
- [53] V. Zardetto, B. L. Williams, A. Perrotta, F. Di Giacomo, M. A. Verheijen, R. Andriessen, W. M. M. Kessels, M. Creatore, *Sustainable Energy Fuels* **2017**, *1*, 30.
- [54] J. A. Raiford, S. T. Oyakhire, S. F. Bent, *Energy Environ. Sci.* **2020**, *13*, 1997.
- [55] J. Li, R. Xia, W. Qi, X. Zhou, J. Cheng, Y. Chen, G. Hou, Y. Ding, Y. Li, Y. Zhao, X. Zhang, *J. Power Sources* **2021**, *485*, 229313.
- [56] F. J. Ramos, T. Maindron, S. Béchu, A. Rebai, M. Frégnaux, M. Bouttemy, J. Rousset, P. Schulz, N. Schneider, *Sustainable Energy Fuels* **2018**, *2*, 2468.
- [57] Y. Il Lee, N. J. Jeon, B. J. Kim, H. Shim, T. Y. Yang, S. Il Seok, J. Seo, S. G. Im, *Adv. Energy Mater.* **2018**, *8*, 1701928.
- [58] L. Hoffmann, D. Theirich, S. Pack, F. Kocak, D. Schlamm, T. Hasselmann, H. Fahl, A. Raupke, H. Gargouri, T. Riedl, *ACS Appl. Mater. Interfaces* **2017**, *9*, 4171.
- [59] R. D. Raninga, R. A. Jagt, S. Béchu, T. N. Huq, W. Li, M. Nikolka, Y. H. Lin, M. Sun, Z. Li, W. Li, M. Bouttemy, M. Frégnaux, H. J. Snaith, P. Schulz, J. L. MacManus-Driscoll, R. L. Z. Hoye, *Nano Energy* **2020**, *75*, 104946.
- [60] L. Hoffmann, K. O. Brinkmann, J. Malerczyk, D. Rogalla, T. Becker, D. Theirich, I. Shutsko, P. Görrn, T. Riedl, *ACS Appl. Mater. Interfaces* **2018**, *10*, 6006.
- [61] Y. Lv, P. Xu, G. Ren, F. Chen, H. Nan, R. Liu, D. Wang, X. Tan, X. Liu, H. Zhang, Z. K. Chen, *ACS Appl. Mater. Interfaces* **2018**, *10*, 23928.

- [62] H. Klumbies, P. Schmidt, M. Hähnel, A. Singh, U. Schroeder, C. Richter, T. Mikolajick, C. Hoßbach, M. Albert, J. W. Bartha, K. Leo, L. Müller-Meskamp, *Org. Electron.* **2015**, *17*, 138.
- [63] M. D. Groner, S. M. George, R. S. McLean, P. F. Carcia, *Appl. Phys. Lett.* **2006**, *88*, 051907.
- [64] E. Kim, Y. Han, W. Kim, K. C. Choi, H. G. Im, B. S. Bae, *Org. Electron.* **2013**, *14*, 1737.
- [65] K. L. Jarvis, P. J. Evans, *Thin Solid Films* **2017**, *624*, 111.
- [66] C. Besleaga, L. E. Abramiuc, V. Stancu, A. G. Tomulescu, M. Sima, L. Trinca, N. Plugaru, L. Pintilie, G. A. Nemnes, M. Iliescu, H. G. Svavarsson, A. Manolescu, I. Pintilie, *J. Phys. Chem. Lett.* **2016**, *24*, 5168.
- [67] X. Wang, S. Shen, Z. Feng, C. Li, *Chin. J. Catal.* **2016**, *37*, 2059.
- [68] J. Shi, J. Chen, Z. Feng, T. Chen, Y. Lian, X. Wang, C. Li, *J. Phys. Chem. C* **2007**, *111*, 693.
- [69] S. Masubuchi, E. Watanabe, Y. Seo, S. Okazaki, T. Sasagawa, K. Watanabe, T. Taniguchi, T. Machida, *npj 2D Mater. Appl.* **2020**, *4*, 3.
- [70] S. Liu, C. N. Melton, S. Venkatakrisnan, R. J. Pandolfi, G. Freychet, D. Kumar, H. Tang, A. Hexemer, D. M. Ushizima, *MRS Commun.* **2019**, *9*, 586.
- [71] G. B. Goh, A. Vishnu, C. Siegel, N. Hodas, in *KDD '18 Proc. of the 24th ACM SIGKDD Int. Conf. on Knowledge Discovery and Data Mining*, Vol. 1, ACM, New York **2018**, p. 302.
- [72] A. Krizhevsky, I. Sutskever, G. E. Hinton, *Commun. ACM* **2017**, *60*, 84.
- [73] S. Seo, S. Jeong, C. Bae, N. G. Park, H. Shin, *Adv. Mater.* **2018**, *30*, 1801010.
- [74] R. Singh, S. Ghosh, A. S. Subbiah, N. Mahuli, S. K. Sarkar, *Sol. Energy Mater. Sol. Cells* **2020**, *205*, 110289.
- [75] C. Y. Chang, K. T. Lee, W. K. Huang, H. Y. Siao, Y. C. Chang, *Chem. Mater.* **2015**, *27*, 5122.
- [76] S. J. Kim, S. H. Yong, Y. J. Choi, H. Hwangbo, W.-Y. Yang, H. Chae, *J. Vac. Sci. Technol., A* **2020**, *38*, 022418.